INTERNATIONAL JOURNAL FOR NUMERICAL METHODS IN FLUIDS
Int. J. Numer. Meth. Fluids 0000; **00**:1–25
Published online in Wiley InterScience (www.interscience.wiley.com). DOI: 10.1002/fld

Some considerations for high-order 'incremental remap'-based transport schemes: edges, reconstructions and area integration

Paul Aaron Ullrich[1]*, Peter Hjort Lauritzen[2] and Christiane Jablonowski[1]

[1]*Department of Atmospheric, Oceanic and Space Sciences, Space Research Building, University of Michigan, 2455 Hayward St., Ann Arbor MI 48109. E-mail: paullric@umich.edu* [2]*Climate and Global Dynamics Division, National Center for Atmospheric Research, Boulder, CO.*

SUMMARY

The problem of 2D tracer advection on the sphere is extremely important in modeling of geophysical fluids, and has been tackled using a variety of approaches. A class of popular approaches for tracer advection include 'incremental remap' or cell-integrated semi-Lagrangian-type schemes. These schemes achieve high-order accuracy without the need for multi-stage integration in time, are capable of large time steps and tend to be more efficient than other high-order transport schemes when applied to a large number of tracers over a single velocity field.

In this paper the simplified flux-form implementation of the Conservative Semi-LAgrangian Multi-tracer scheme (CSLAM) is reformulated using quadratic curves to approximate the upstream flux volumes and Gaussian quadrature for integrating the edge flux. The high-order treatment of edge fluxes is motivated due to poor accuracy of the CSLAM scheme in the presence of strong nonlinear shear, such as one might observe in the midlatitudes near an atmospheric jet. Without the quadratic treatment of upstream edges we observe at most second-order accuracy under convergence of grid resolution, which is returned to third-order accuracy under the improved treatment. A shallow-water barotropic instability also reveals clear evidence of grid imprinting without the quadratic correction. Consequently, these tests reveal a problem which might arise in tracer transport near nonlinearly sheared regions of the real atmosphere, particularly near cubed-sphere panel edges. Although CSLAM is used as the foundation for this analysis, the conclusions of this paper are applicable to the general class of incremental remap schemes.

Received ...

KEY WORDS: Conservative transport; cubed-sphere; finite-volume; incremental remap; flux-form semi-Lagrangian; multi-tracer transport

1. INTRODUCTION

The problem of 2D tracer advection is extremely important in all branches of atmospheric science, yet it can be formulated very simply via the mass continuity equation

$$\frac{\partial \psi}{\partial t} + \nabla \cdot (\psi \mathbf{u}) = 0, \tag{1}$$

Table I. Approaches taken for incremental remapping under the CSLAM framework. The quadrature-based formulations use Gaussian quadrature over an upstream flux volume to compute total flux through an edge, whereas all other schemes use boundary integrals for computing the mass in the upstream region or flux volume.

Version	Flux-Form	Simplified Fluxes	Edges	Reference
Standard			Linear	[3]
Traditional flux-form	✓		Linear	[2, 4]
Simplified flux-form	✓	✓	Linear	[8, 5]
Quadrature-based	✓	✓	Linear	Section 2.4
Quadrature-based with quadratic edges	✓	✓	Quadratic	Section 2.5
Simplified with quadratic edges	✓	✓	Quadratic	Section 2.6

where ψ is a passive density variable and $\mathbf{u}$ is the velocity vector. Solving this equation accurately while maintaining desirable properties such as positivity or tracer correlation is extremely challenging [1]. Nonetheless, the incremental remap / semi-Lagrangian scheme of [2] is one approach that has been shown to be largely successful at tackling the advection problem. More recently, the Conservative Semi-LAgrangian Multi-tracer scheme (CSLAM) has been proposed by [3], followed by the flux-form formulation of [4] and the simplified flux-form formulation of [5]. CSLAM has been demonstrated to be very effective at accurately solving the advection equation on the cubed-sphere [6], and is in the process of being implemented in the spectral element dynamical core of the National Center for Atmospheric Research (NCAR) Community Atmosphere Model (CAM) [7]. For reference, we provide details of the various implementations of the CSLAM scheme in Table I.

Under the traditional finite-volume semi-Lagrangian approach, the tracer mass contained in element $\mathcal{Z}_k$ is determined by tracing nodal trajectories backwards in time to an upstream source element $\mathbf{a}_k$ (see Figure 1a,b). The total mass within the upstream source element is then determined by integration over $\mathbf{a}_k$ using a mass distribution obtained from the sub-grid-scale reconstruction at the previous time step. Under this formulation, (1) is effectively discretized as

$$\bar{\bar{\psi}}_k^{n+1} = \frac{1}{|\mathcal{Z}_k|} \int_{\mathbf{a}_k} \psi^n(\mathbf{x}) dV, \tag{2}$$

where $\bar{\bar{\psi}}_k^{n+1}$ denotes the element average of ψ in element $\mathcal{Z}_k$ at time step $n+1$, $|\mathcal{Z}_k|$ is the volume of element $\mathcal{Z}_k$, dV is the volume element over the coordinate $\mathbf{x}$ and $\psi^n(\mathbf{x})$ denotes some continuous representation of the scalar density field ψ at time step n.

Under the flux-form approach of [2] we instead trace nodal trajectories backwards in time for each edge so as to form a *flux volume*. Integrating the total tracer mass within a flux volume then yields the total flux through that edge. In this case, the integration must be performed for each edge of $\mathcal{Z}_k$ (see Figure 1c-f). The continuity equation (1) then takes the form

$$\bar{\bar{\psi}}_k^{n+1} = \bar{\bar{\psi}}_k^{n} + \frac{1}{|\mathcal{Z}_k|} \left[F_E + F_N + F_W + F_S \right], \tag{3}$$

Prepared using fldauth.cls
DOI: 10.1002/fld

where F_E is the mass flux into the element through the east edge, and similarly for the north, west and south edges. The fluxes are computed by integrating over the flux volumes, *i.e.* for the east edge we have

$$F_E = \sigma \int_{\mathbf{a}_k^{(E)}} \psi^n(\mathbf{x}) dV, \tag{4}$$

where $\sigma \in \{-1, 1\}$ is a sign indicator which depends on whether the flux is outward or inward. The flux is defined analogously for all other edges. Traditionally, the integration procedure involves identifying overlap areas between quadrilateral flux-areas and the static Eulerian grid, which is generally a non-trivial problem. If the choice of $\psi^n(\mathbf{x})$ is the same as in (2) then the traditional semi-Lagrangian approach is equivalent to the flux-form semi-Lagrangian approach. However, under the swept-area approach of [8] one simply uses the sub-grid-scale reconstruction in the two elements which directly neighbor the edge. Perhaps surprisingly, the resulting simplified scheme was shown in [5] to improve accuracy for sufficiently small Courant numbers. However, this modification also imposes conditions on the stability of the advection scheme (in our case we require the Courant number ≤ 1). This restriction is generally adequate for tracer transport in atmospheric models where the advective CFL condition is much weaker than the CFL condition imposed on the dynamics. In this paper we continue the work of [5] and pursue the simplified approach to integrating flux areas. Consequently, the integration procedure is relatively straightforward since we do not need to isolate overlaps between the flux volume and neighboring elements.

The purpose of this paper is twofold. First, we formulate the flux-form semi-Lagrangian transport scheme of [4] using quadrature for computing edge fluxes. An improved treatment of the upstream flux region is achieved by using quadratic functions for representing the edges of this region. The modification is presented for both quadrature and line integral based formulations of the CSLAM scheme. We argue that the added cost of this adjustment is small when multiple tracers are being transported. Second, we present two test cases to demonstrate the rationale for our improved treatment. The first test is a steady nonlinearly sheared flow which is designed to mimic a mid-latitudinal atmospheric jet. In this case the quadratic correction is shown to be necessary for the numerical method to achieve the expected third-order accurate convergence with grid refinement. The second test is a shallow-water barotropic instability which shows clear evidence of grid imprinting without the quadratic correction. Consequently, we suspect that these tests reveal a problem which might arise in tracer transport near regions of strong nonlinear shear in the real atmosphere. Although CSLAM is used as the foundation for this analysis, the conclusions of this paper are applicable to the general class of incremental remap schemes, particularly on the cubed-sphere grid.

The paper is structured as follows. In section 2 we present our formulation of the semi-Lagrangian transport scheme, including a description of the quadratic correction to the flux volumes. The results from testing our improved formulation are given in section 3, and conclusions are discussed in section 4. For completeness, the reconstruction strategy we have used is presented in appendix A, and includes a description of our methodology for filtering the reconstruction.

DOI: 10.1002/fld

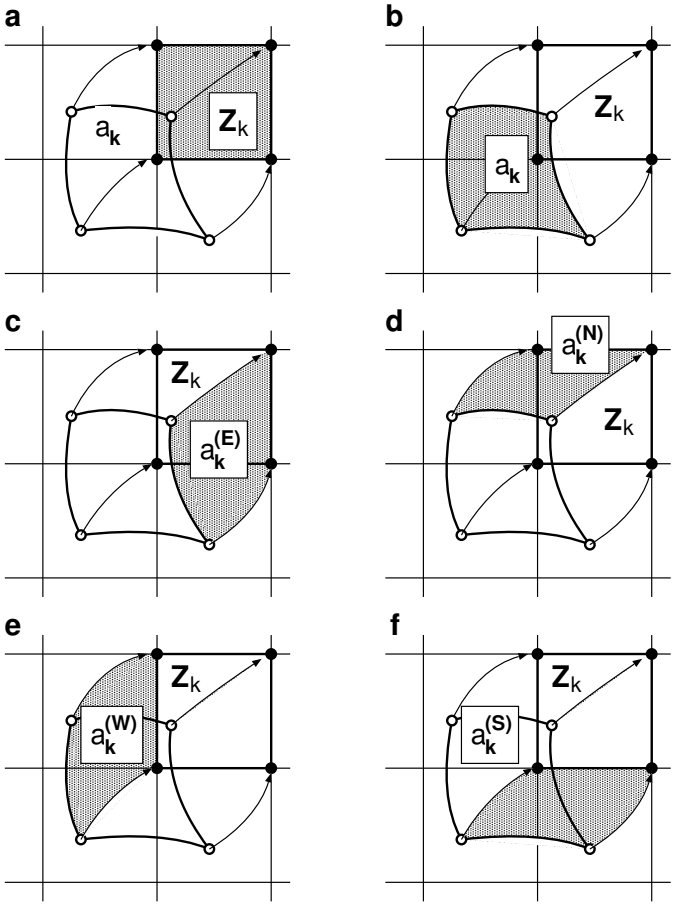

Figure 1. An illustration of the semi-Lagrangian approach. The nodes of element $\mathcal{Z}_k$ (**a**) are tracked upstream to element $\mathbf{a}_k$ (**b**). Under the traditional semi-Lagrangian formulation, the tracer mass within element $\mathbf{a}_k$ is obtained by directly integrating $\mathbf{a}_k$. Under the flux-form formulation we instead integrate over flux areas for the (**c**) east $\mathbf{a}_k^{(E)}$, (**d**) north $\mathbf{a}_k^{(N)}$, (**e**) west $\mathbf{a}_k^{(W)}$ and (**f**) south $\mathbf{a}_k^{(S)}$ face. The original element (**a**) minus the sum of all flux area masses (**c**-**f**) is equal to the mass in the upstream element $\mathbf{a}_k$, regardless of the trajectory.

2. CONSERVATIVE SEMI-LAGRANGIAN ADVECTION ON THE CUBED-SPHERE

In this section we present our improvements to the simplified flux-form CSLAM scheme, including the quadrature-based formulation of the scheme and the quadratic treatment of the upstream flux region. Some notation which is important for models on the cubed-sphere grid is introduced in section 2.1, and will be used throughout this paper. Our approach for high-order tracking of nodal trajectories is described in 2.2. The simplified flux-form approach is introduced in section 2.3 and the quadrature formulation of CSLAM follows in section 2.4. In sections 2.5 and 2.6 we present an improved treatment of upstream flux edges for the quadrature and line integral formulations of CSLAM. Some additional discussion comparing the conditioning of the quadrature and line integral formulations is given in section 2.7.

Prepared using fldauth.cls
DOI: 10.1002/fld

Table II. Properties of the cubed sphere grid for different resolutions. Here Δx is the grid spacing at the equator, $RLL_{equatorial}$ denotes the grid spacing (in degrees) on a regular latitude-longitude grid with the same equatorial spacing as the cubed-sphere grid and RLL_{equiv} denotes the equivalent grid spacing (in degrees) on the regular latitude-longitude grid with the same number of elements. The accuracy of the model is most closely linked to $RLL_{equatorial}$, whereas RLL_{equiv} represents the resolution required for a similar run-time.

Resolution	Δx	$RLL_{equatorial}$	RLL_{equiv}
c60	165 km	1.50°	1.73°
c120	82.5 km	0.75°	0.87°
c160	62.5 km	0.56°	0.65°
c240	41.3 km	0.38°	0.43°
c480	20.6 km	0.19°	0.22°

2.1. Coordinates on the cubed-sphere

The cubed-sphere grid, as described by [9] and [10], consists of six Cartesian patches arranged along the faces of a cube, which is then 'inflated' to fill a spherical shell. On the equiangular cubed-sphere grid, coordinates are given as (α, β, n_p), with central angles $\alpha, \beta \in [-\frac{\pi}{4}, \frac{\pi}{4}]$ and panel index $n_p \in \{1, 2, 3, 4, 5, 6\}$. By convention, we choose panels $1-4$ to be along the equator and panels 5 and 6 to be centered on the northern and southern pole, respectively. Gnomonic coordinates are related to equiangular coordinates via the transform

$$X = \tan\alpha, \qquad Y = \tan\beta. \tag{5}$$

Gnomonic coordinates are particularly useful since any straight line in gnomonic coordinates is also a great circle arc. Further, integration over regions in gnomonic coordinates is typically much simpler than in equiangular coordinates.

The discrete resolution of the cubed-sphere is typically written in the form $c\langle N_c\rangle$, where each coordinate direction consists of N_c grid elements. Hence, the total number of grid elements on the cubed-sphere is $N_c \times N_c \times 6$. Grid elements on a particular panel are denoted by $\mathcal{Z}_{i,j}$ with indices $(i, j) \in [0, \ldots, N_c - 1]^2$, which denote the region bounded by

$$\alpha \in \left[i\Delta\alpha - \frac{\pi}{4}, (i+1)\Delta\alpha - \frac{\pi}{4}\right], \qquad \beta \in \left[j\Delta\alpha - \frac{\pi}{4}, (j+1)\Delta\alpha - \frac{\pi}{4}\right], \tag{6}$$

where on an equiangular grid, the grid spacing is

$$\Delta\alpha = \pi/(2N_c). \tag{7}$$

Equiangular element center points are defined for each element as the point $\boldsymbol{\alpha}_{i,j} = (\alpha_i, \beta_j)$ with

$$\alpha_i = \left(i + \frac{1}{2}\right)\Delta\alpha - \frac{\pi}{4}, \qquad \beta_j = \left(j + \frac{1}{2}\right)\Delta\alpha - \frac{\pi}{4}. \tag{8}$$

The gnomonic element center points are then defined as $\mathbf{X}_{i,j} = (X_i, Y_j)$ with $X_i = \tan\alpha_i$ and $Y_j = \tan\beta_j$. Some properties of the cubed-sphere grid for a variety of resolutions are given in Table II.

Prepared using fldauth.cls
DOI: 10.1002/fld

2.2. Computing Backward Trajectories

In order to compute backward trajectories for each of the nodal points, one must solve the Lagrangian transport equation for a point,

$$\frac{d\mathbf{x}}{dt} = \mathbf{u}. \tag{9}$$

When the analytic velocity field is known this equation can often be integrated analytically to obtain the origin of each point on the mesh. If the velocity field is only known discretely, this equation must instead be solved numerically. Accurate representation of upstream areas requires a high-order solution of this equation, or else the quality of the final solution will be degraded. For example, [6] Table 3 demonstrates that a low-order trajectory algorithm can dramatically increase error norms for certain non-linear flows. One high-order approach which we propose here relies on solving (9) via a fourth-order Runge-Kutta time integrator. In this case, we have

$$\mathbf{x}^{(1)} = \mathbf{x}_0 - \frac{\Delta t}{2}\mathbf{u}\left(\mathbf{x}_0, t^{n+1}\right), \tag{10}$$

$$\mathbf{x}^{(2)} = \mathbf{x}_0 - \frac{\Delta t}{2}\mathbf{u}\left(\mathbf{x}^{(1)}, t^{n+1} - \frac{\Delta t}{2}\right), \tag{11}$$

$$\mathbf{x}^{(3)} = \mathbf{x}_0 - \Delta t\mathbf{u}\left(\mathbf{x}^{(2)}, t^{n+1} - \frac{\Delta t}{2}\right), \tag{12}$$

$$\mathbf{x}^{(4)} = -\frac{1}{3}\mathbf{x}_0 + \frac{1}{3}\mathbf{x}^{(1)} + \frac{2}{3}\mathbf{x}^{(2)} + \frac{1}{3}\mathbf{x}^{(3)} - \frac{\Delta t}{6}\mathbf{u}\left(\mathbf{x}^{(3)}, t^{n}\right). \tag{13}$$

Consequently the point $\mathbf{x}^{(4)}$ is a fourth-order approximation to the point at time t^n, which under Lagrangian advection, would have ended up at $\mathbf{x}_0$ at time $t^{n+1} = t^n + \Delta t$. Other methods for solving (9) are also available, such as the approach of [11] or the low-order approaches described in [12]. Although the accuracy requirements for computing the trajectories do impose some additional expense, the corresponding trajectories must only be computed once per time step for all tracers.

2.3. The Simplified Flux-Form Transport Scheme

Once the backward trajectories have been computed for each edge, the flux across the edge can be computed by integrating over the flux region. There are several possible valid arrangements of nodal points (depending on the flow field) that determine the flux region, as depicted in Figure 2. This figure depicts an edge of constant α connecting edge nodes (1,3) and the respective upstream translation of these edge nodes (0,2) (for an edge of constant β the process is analogous, and so is not repeated here). The flux region is then given by the quadrilateral (0,1,3,2). Note that we neglect the possibility of point 0 being above point 2, since this corresponds to very strong divergence in the velocity field that may have arisen due to an instability in the calculation. In this case, the simulation is halted; if such a situation is physical for the specified problem, we suggest reducing the time step accordingly.

Flux across the edge (4) is computed via the integral

$$F = \sigma \int_{\mathbf{a}_k^\tau} \psi(\mathbf{X}) J_{XY}(\mathbf{X}) dX dY, \tag{14}$$

Prepared using fldauth.cls
DOI: 10.1002/fld

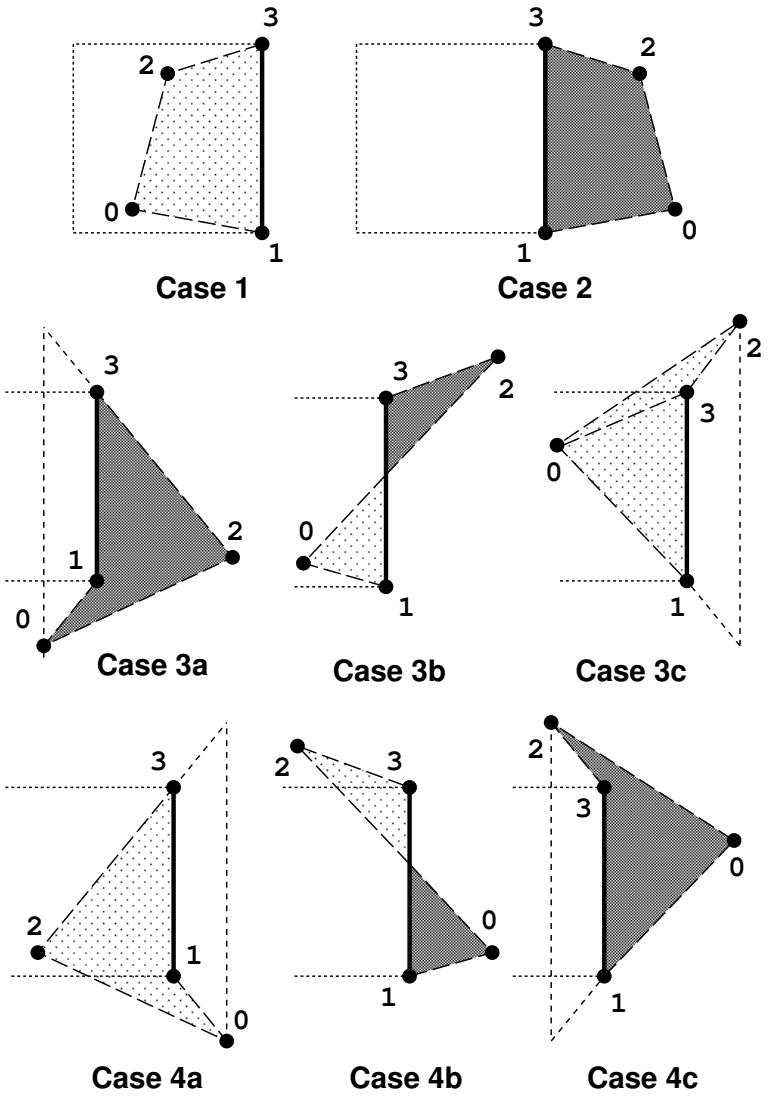

Figure 2. Depiction of each of the cases that must be treated by the flux integration algorithm. The edge (1,3) denotes the edge for which the advective flux is desired. The points 0 and 2 are freely determined by the trajectory computation algorithm. Regions which lead to an outward flux are lightly shaded, whereas regions which lead to an inward flux are heavily shaded. The dotted lines denote the north/south edges of the left element.

where $\mathbf{a}_k^\tau$ denotes an arbitrary flux region. The value of σ is chosen in accordance with the arrangement of nodes: In Figure 2 lightly shaded regions lead to $\sigma = -1$ and heavily shaded regions lead to $\sigma = 1$. Summation is implied over each flux volume if needed, such as in case 3b and 4b. The Jacobian in Gnomonic coordinates is given by J_{XY}, which takes the form

$$J_{XY}(\mathbf{X}) = \frac{1}{(1 + X^2 + Y^2)^{3/2}}. \tag{15}$$

Prepared using fldauth.cls
DOI: 10.1002/fld

In general, the sub-grid-scale reconstruction of ψ in element $\mathcal{Z}_{i,j}$ can be written as

$$\psi_{i,j}(\mathbf{X}) = \sum_{p,q} c_{(p,q)} X^p Y^q, \tag{16}$$

where the summation is taken over all reconstruction coefficients $c_{(p,q)}$. The reconstruction coefficients are used to represent the continuous behavior of ψ within each element and are generally constructed using neighboring element-averages. Our particular choice of reconstruction coefficients is described in the appendix. On substituting (16) into (14) we obtain

$$F = \sigma \sum_{p,q} c_{(p,q)} \int_{\mathbf{a}_k^\tau} X^p Y^q J_{XY}(\mathbf{X}) dX dY, \tag{17}$$

and so effectively reduce the problem of computing the fluxes to a linear combination of the reconstruction coefficients and the integrated Jacobian-weighted polynomial basis functions. Multi-tracer efficiency is attained by utilizing the fact that only the reconstruction coefficients change between tracers, and so the integrals must only be computed once for each pair (p, q).

When the flux edge is also a cubed-sphere panel edge, the integration must be performed on the appropriate panel to ensure consistency. For instance, in case 3b, the light-shaded region is integrated on the left panel and the heavy-shaded region is integrated on the right panel. Under this procedure only one flux is ever computed for each edge and so there are no conservation issues which may arise if the integral is evaluated over the panel's halo region.

2.4. Computing fluxes via quadrature over the flux volume

Several options exist for computing the integrals over the flux volume. Under the quadrature-based formulation, these integrals are computed via an appropriately chosen quadrature rule. For fourth-order accuracy a four-point quadrature rule, such as the one described below, can be used. In case 3 and 4 of Figure 2 the convex property of the quadrilaterals has been lost, and so a single quadrature rule for a quadrilateral is insufficient. Instead, for case 3b and 4b we break the region up into two triangles and, treating the triangles as degenerate quadrilaterals, simply apply the quadrilateral quadrature rule to each triangle. It is worth noting that a fourth-order accurate integration over a triangular region still requires at least four quadrature points, and so there is no significant benefit to choosing a simpler quadrature rule over a triangle. For case 3a, 3c, 4a and 4c the integral is instead over a wedge-shaped region. To integrate over the wedge, we extend the integration region outward to form a triangle-shaped region (short dashed lines) so that the wedge can be viewed as the difference between the triangular region and a convex quadrilateral region. A quadrature rule is then applied to both the triangular region and convex quadrilateral and the difference taken to obtain the integral over the wedge. In using this approach for dividing the flux region, two corner points of our integration domain will always lie along a line of constant X. We will exploit this feature in the definition of our quadrature rule below.

In general, defining high-order and optimal quadrature rules for arbitrarily shaped quadrilaterals is a non-trivial problem. However, by choosing an appropriate, alternative set of coordinates, it is possible to transform our problem into the trivial problem of integration over the unit square. To do so, we introduce coordinates $\mathbf{s} = (s, t) \in [0, 1]^2$ (see Figure 3). On an arbitrary quadrilateral $\mathbf{a}$,

DOI: 10.1002/fld

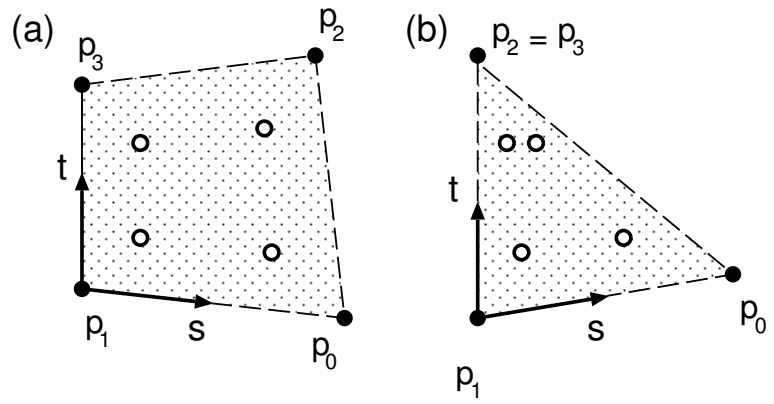

Figure 3. A depiction of the location of quadrature points for (a) quadrilateral and (b) degenerate quadrilateral integration. Nodal points are denoted by $\mathbf{p}_i = (X_i, Y_i)$.

bounded by points $\mathbf{p}_i = (X_i, Y_i)$ with $X_1 = X_3$, these coordinates can be implicitly written as

$$X(\mathbf{s}) = X(s,t) = X_1 + s(bt + c), \qquad Y(\mathbf{s}) = Y(s,t) = Y_1 + fs + (s(g-f) + \Delta X)t, \quad (18)$$

where $b = X_2 - X_0$, $c = X_0 - X_1$, $f = Y_0 - Y_1$, $g = Y_2 - Y_3$ and $\Delta X = Y_3 - Y_1$. Hence, applying integration by substitution, we obtain

$$\int_{\mathbf{a}} \psi(\mathbf{X}) J_{XY}(\mathbf{X}) dX dY = \int_{s=0}^{1} \int_{t=0}^{1} \psi(\mathbf{X}(s,t)) J_{XY}(\mathbf{X}(s,t)) \left| \det \left(\frac{\partial(X,Y)}{\partial(s,t)} \right) \right| dt ds, \quad (19)$$

where

$$\Phi_1(\mathbf{s}) \equiv \left| \det \left(\frac{\partial(X,Y)}{\partial(s,t)} \right) \right| = \left| \det \begin{pmatrix} \frac{\partial X}{\partial s} & \frac{\partial X}{\partial t} \\ \frac{\partial Y}{\partial s} & \frac{\partial Y}{\partial t} \end{pmatrix} \right| = \left| (c(g-f) - bf)s + \frac{(X(\mathbf{s}) - X_1)\Delta X}{s} \right|. \quad (20)$$

This term describes the area adjustment due to deformation of the quadrilateral.

Given an arbitrary quadrature rule with quadrature points $\mathbf{s}_k = (s_k, t_k)$ and associated weights w_k, the numerical integral is then computed via

$$\int_{\mathbf{a}} X^p Y^q J_{XY} dX dY = \sum_k X(\mathbf{s}_k)^p \, Y(\mathbf{s}_k)^q \, J_{XY}(\mathbf{X}(\mathbf{s}_k)) \, \Phi_1(\mathbf{s}_k) \, w_k. \quad (21)$$

For quadrilateral integration we use a four-point fourth-order quadrature rule (see Figure 3) given by

$$\mathbf{s}_1 = \left(-\frac{1}{\sqrt{3}}, -\frac{1}{\sqrt{3}} \right), \quad \mathbf{s}_2 = \left(\frac{1}{\sqrt{3}}, -\frac{1}{\sqrt{3}} \right), \quad \mathbf{s}_3 = \left(-\frac{1}{\sqrt{3}}, \frac{1}{\sqrt{3}} \right), \quad \mathbf{s}_4 = \left(\frac{1}{\sqrt{3}}, \frac{1}{\sqrt{3}} \right), \quad (22)$$

and $w_i = 1/4$ for each $i \in \{1, 2, 3, 4\}$.

Prepared using fldauth.cls
DOI: 10.1002/fld

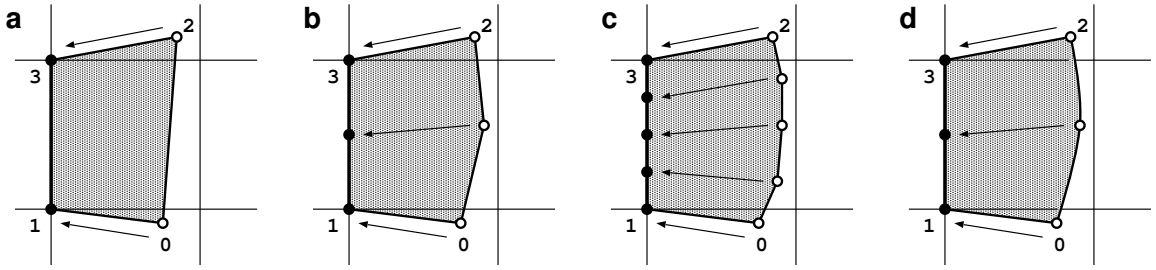

Figure 4. A depiction of various methods for constructing upstream edges. (a) The flux region is approximated as a quadrilateral with the upstream edge approximated by a single line segment. (b) A slightly more accurate approximation to the upstream edge, obtained by inserting one additional point midway along the edge $(1,3)$ and tracing the trajectory backwards. In this case, straight line segments are still used to approximate the upstream edge. (c) Further refinement of the upstream edge by inserting additional points along $(1,3)$ and calculating backwards trajectories. (d) An upstream edge approximated by fitting a quadratic through three trajectory points.

2.5. A quadratic treatment of edges

So far, all of our discussion has assumed that the flux region can be represented as a combination of convex quadrilaterals and triangles. In [3] it was speculated that additional points along each edge of the flux region could be used to improve the overall accuracy of the method. The authors suggested that a more accurate flux region could be constructed by connecting the new flux points via additional line segments (see Figure 4a-c), but their choice of idealized test cases showed only a negligible or very minor improvement in error norms under this approach. Note that additional line segments do not actually increase the formal order-of-accuracy of the representation of the flux region, since any number of line segments will only ever be a second-order accurate to the true upstream edge. Further, the addition of extra points along each trajectory generally does not improve model accuracy, since these points will not affect the Lagrangian upstream area (see [1]).

In this paper, we propose an alternative form for the bounding region of the flux domain. Under the modified approach, the upstream projection of the flux edge is approximated via a quadratic curve (see Figure 4d). The construction of this quadratic curve requires an additional nodal value, which we obtain by computing the backwards trajectory of point $\mathbf{p}_5$ to obtain $\mathbf{p}_4$, as in Figure 5.

Applying the same approach as in section 2.4, we define coordinates $(s,t) \in [0,1]^2$ via

$$X(\mathbf{s}) = X(s,t) = X_1 + s(a^2 t + bt + c), \qquad Y(\mathbf{s}) = Y(s,t) = Y_1 + fs + (s(g-f) + \Delta X)t. \tag{23}$$

Observe that (23) is identical to (18) except with the addition of the quadratic term $a^2 st$ to the X coordinate. This modification leads to a deformational term that takes the form

$$\Phi_2(\mathbf{s}) \equiv \left| \det \left(\frac{\partial(X,Y)}{\partial(s,t)} \right) \right| = \left| (-a(g-f)t^2 - 2aft - bf + c(g-f))s + \frac{(X(\mathbf{s}) - X_1)\Delta X}{s} \right|. \tag{24}$$

The quadratic coefficients (a,b,c) are defined by fitting a quadratic through points

$$(t,X) = \{(0, X_0 - X_1), (t_*, X_4 - X_1), (1, X_2 - X_1)\}, \quad \text{with} \quad t_* = \frac{Y_4 - Y_0}{Y_2 - Y_0}. \tag{25}$$

Prepared using fldauth.cls
DOI: 10.1002/fld

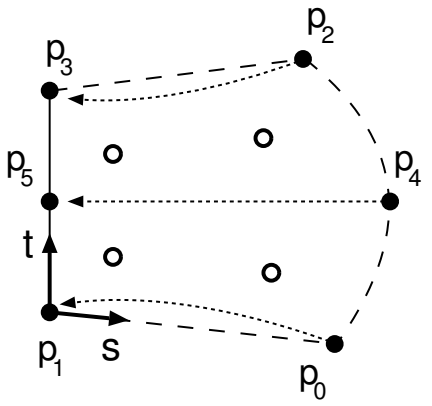

Figure 5. The location of quadrature points (empty circles) for an element with the quadratic correction applied to the upstream flux edge. The points $\mathbf{p}_0$, $\mathbf{p}_2$, $\mathbf{p}_4$ and track upstream to $\mathbf{p}_1$, $\mathbf{p}_3$ and $\mathbf{p}_5$, respectively.

This choice leads to

$$a = \frac{X_2 t_* - X_4 + X_0(1-t_*)}{t_*(1-t_*)}, \tag{26}$$

$$b = \frac{X_4 - X_0 + t_*^2(X_0 - X_2)}{t_*(1-t_*)}, \tag{27}$$

$$c = X_0 - X_1. \tag{28}$$

This construction requires that $Y_0 \neq Y_2$, $Y_2 \neq Y_4$ and $Y_0 \neq Y_4$ which should not occur for sufficiently laminar flows and small enough Courant number.

As will be demonstrated in section 3, the quadratic treatment is useful for problems where the divergence errors (that is, the errors made by approximating the upstream flux region) overwhelm the errors due to the sub-grid-scale reconstruction. These situations generally arise in the presence of a strong horizontal shear in the flow, such as a midlatitudinal jet. In this case, the convergence rate of the numerical method is expected to drop to second-order accuracy, which is consistent with a linear approximation.

The added cost of the quadratic treatment is potentially significant, since an additional trajectory must be computed along the midpoint of every edge. This choice nearly triples the number of trajectories that must be computed at each time step. However, we emphasize that these additional computations must only be performed once per time step, regardless of the number of tracer species. For a large number of tracers this added cost is generally small compared to the cost of computing the reconstruction coefficients.

2.6. The line-integral formulation of the quadratic correction

In this section we present the quadratic treatment of flux edges for schemes which calculate the integrals of (17) via boundary integration, such as the methods described by [4] and [5]. By appropriately choosing a set of geometric potentials $\mathbf{F}_{(p,q)}$ such that

$$\nabla \cdot \mathbf{F}_{(p,q)} = X^p \, Y^q \, J_{XY}(\mathbf{X}), \tag{29}$$

DOI: 10.1002/fld

we can use Gauss' divergence theorem to rewrite the geometric integrals in (17) as line integrals around the boundary $\partial\mathbf{a}_k$ of $\mathbf{a}_k$ via

$$\int_{\mathbf{a}_k} X^p Y^q J_{XY}(\mathbf{X}) dX dY = \int_{\mathbf{a}_k} \nabla \cdot \mathbf{F} dX dY = \oint_{\partial \mathbf{a}_k} \mathbf{F} \cdot d\mathbf{S}, \tag{30}$$

where $d\mathbf{S}$ denotes the length-weighted normal vector to the boundary. Traditionally, $\mathbf{F}$ is chosen such that $\mathbf{F} = (F_x, 0)$; that is, $\mathbf{F}$ has no component in the Y direction. This simplifies the resulting integration and leads to a unique potential $\mathbf{F}_{(p,q)}$ for each pair (p, q). The boundary integral is usually evaluated by splitting the integral up into four line integrals along each segment of the flux volume, such as

$$\oint_{\partial \mathbf{a}_k} \mathbf{F} \cdot d\mathbf{S} = \underbrace{\int_{\mathbf{X}_0\mathbf{X}_2} \mathbf{F} \cdot d\mathbf{S}}_{\text{Upstream flux edge}} + \underbrace{\int_{\mathbf{X}_2\mathbf{X}_3} \mathbf{F} \cdot d\mathbf{S}}_{\text{Upper trajectory}} + \underbrace{\int_{\mathbf{X}_3\mathbf{X}_1} \mathbf{F} \cdot d\mathbf{S}}_{\text{Flux edge}} + \underbrace{\int_{\mathbf{X}_1\mathbf{X}_0} \mathbf{F} \cdot d\mathbf{S}}_{\text{Lower trajectory}}. \tag{31}$$

Each of these line integrals fall into three possible cases: (1) a straight line segment of any orientation, (2) a quadratic upstream flux edge generated by a line of constant α or (3) a quadratic upstream flux edge generated by a line of constant β. The algorithm for integrating along each of these line segments is described below.

Case 1: Any arbitrary line segment connecting points $\mathbf{X}_i = (X_i, Y_i)$ and $\mathbf{X}_j = (X_j, Y_j)$ can be parameterized as

$$\mathbf{X}(t) = \mathbf{X}_i + (\mathbf{X}_j - \mathbf{X}_i)t, \tag{32}$$

for which we observe

$$d\mathbf{S} = ((Y_j - Y_i), -(X_j - X_i))dt. \tag{33}$$

Then the line integral takes the form

$$\int_{\mathbf{X}_i\mathbf{X}_\mathbf{j}} \mathbf{F} \cdot d\mathbf{S} = (Y_j - Y_i) \int_{t=0}^{1} F_x(\mathbf{X}(t)) dt. \tag{34}$$

Case 2: A quadratic upstream flux edge connecting points $\mathbf{X}_0 = (X_0, Y_0)$, $\mathbf{X}_4 = (X_4, Y_4)$ and $\mathbf{X}_2 = (X_2, Y_2)$ and generated by a line of constant α will take the form

$$X = a(Y - Y_0)^2 + b(Y - Y_0) + c, \tag{35}$$

where the quadratic coefficients (a, b, c) are

$$\begin{aligned} a &= \frac{X_0(Y_4 - Y_2) + X_4(Y_2 - Y_0) + X_2(Y_0 - Y_4)}{(Y_4 - Y_0)(Y_2 - Y_0)(Y_4 - Y_2)}, \\ b &= \frac{X_0((Y_2 - Y_0)^2 - (Y_4 - Y_0)^2) - X_4(Y_2 - Y_0)^2 + X_2(Y_4 - Y_0)^2}{(Y_4 - Y_0)(Y_2 - Y_0)(Y_4 - Y_2)}, \\ c &= X_0. \end{aligned}$$

Prepared using fldauth.cls
DOI: 10.1002/fld

The curve is then parameterized as

$$Y(t) = Y_0 + (Y_2 - Y_0)t, \qquad X(t) = a(Y(t) - Y_0)^2 + b(Y(t) - Y_0) + c. \tag{36}$$

Differentiating with respect to t yields the length-weighted tangent vector

$$\mathbf{t} = ((2at(Y_2 - Y_0) + b)(Y_2 - Y_0), (Y_2 - Y_0)), \tag{37}$$

and hence the length-weighted normal vector

$$d\mathbf{S} = (Y_2 - Y_0)(1, -(2aY(t) + b))dt. \tag{38}$$

The line integral in this case can then be written as

$$\int_{\mathbf{X_a X_4 X_2}} \mathbf{F} \cdot d\mathbf{S} = (Y_4 - Y_0) \int_{t=0}^{1} F_x(\mathbf{X}(t))dt. \tag{39}$$

Hence, for this case the integrand matches (34). However, these two formulations still differ in the position at which the geometric potential F_x is evaluated.

Case 3: A quadratic upstream flux edge connecting points $\mathbf{X}_0 = (X_0, Y_0)$, $\mathbf{X}_4 = (X_4, Y_4)$ and $\mathbf{X}_2 = (X_2, Y_2)$ and generated by a line of constant β will take the form

$$Y = a(X - X_0)^2 + b(X - X_0) + c, \tag{40}$$

where the quadratic coefficients (a, b, c) are

$$\begin{aligned} a &= \frac{Y_0(X_4 - X_2) + Y_4(X_2 - X_0) + Y_2(X_0 - X_4)}{(X_4 - X_0)(X_2 - X_0)(X_4 - X_2)}, \\ b &= \frac{Y_0((X_2 - X_0)^2 - (X_4 - X_0)^2) - Y_4(X_2 - X_0)^2 + Y_2(X_4 - X_0)^2}{(X_4 - X_0)(X_2 - X_0)(X_4 - X_2)}, \\ c &= Y_0. \end{aligned}$$

The curve is then parameterized as

$$X(t) = X_0 + (X_2 - X_0)t, \qquad Y(t) = aX(t)^2 + bX(t) + c. \tag{41}$$

Differentiating with respect to t yields the length-weighted tangent vector

$$\mathbf{t} = ((X_2 - X_0), (2aX(t) + b)(X_2 - X_0)), \tag{42}$$

which leads to a length-weighted normal of the form

$$d\mathbf{S} = (X_2 - X_0)(2at(X_3 - X_1) + b, -1). \tag{43}$$

Prepared using fldauth.cls
DOI: 10.1002/fld

Hence, the line integral will take the form

$$\int_{\mathbf{X}_1\mathbf{X}_2\mathbf{X}_3} \mathbf{F} \cdot d\mathbf{S} = (X_3 - X_1) \int_{t=0}^{1} F_x(\mathbf{X}(t))(2at(X_3 - X_1) + b)dt. \tag{44}$$

Numerically, Gaussian quadrature is used for evaluating each line integral. For fourth-order accuracy two Gaussian quadrature points are used along each edge, requiring eight Gaussian quadrature points in total for each flux volume. In practice, slight asymmetries are known to arise when we choose the geometric potential to be of the form $\mathbf{F} = (F_x, 0)$ since the X and Y coordinate directions are treated differently. This problem can be alleviated by a more symmetric choice of the flux potential.

2.7. Conditioning of quadratic and line-integral formulations

In general, the error norms for both the quadrature-based and line integral formulations of CSLAM match very closely at low resolutions. However, at sufficiently high resolutions (the resolution at which this occurs seems to be problem specific), an error arises in the line integral formulation which appears to be due to nearly exact cancellation of the components of the boundary integral (30). At high resolutions the poor conditioning of the line integral formulation seems to increase the minimum achievable error to above machine truncation, and so leads to poor convergence behavior. Improvements in the conditioning of the line integral approach may be achieved by an intelligent choice of geometric potentials, but this problem is not tackled in this paper. When comparing the simplified flux-form implementation using line integrals and quadrature in terms of efficiency, the quadrature-based formulation also tends to outperform the line integral formulation.

Notably, the line integral formulation is the only approach known to the authors that admits large time steps while maintaining conservation properties of the method [3]. That is, under the line integral formulation integration is performed around the boundary of upstream volumes, and so any deformation of these volumes leads directly to exchange of mass with neighboring elements. Further, since the upstream volumes are non-overlapping and span the entire domain all mass is accounted for during integration.

3. NUMERICAL RESULTS

We now present results from two test cases which arise from a strong nonlinearly sheared flow. In section 3.1 we present a steady nonlinearly sheared zonal flow, and demonstrate that without the quadratic correction the standard CSLAM scheme will attain at most second-order accuracy. A more realistic barotropic instability test is discussed in section 3.2, using the flow field of [13]. This test reveals clear grid imprinting caused by the second-order treatment of upstream flux volumes even at high spatial resolution. No explicit filtering of the reconstruction is applied for these tests, as it does not impact the observed results.

DOI: 10.1002/fld

3.1. Steady Nonlinearly Sheared Zonal Flow

3.1.1. Test case formulation. Test case 3 of [14] makes use of a compact nonlinearly sheared jet which is isolated to the northern hemisphere. In terms of latitude θ and longitude λ, their velocity field takes the form

$$u_\lambda(\lambda,\theta) = u_0 b(x(\theta)) b(x_e - x(\theta)) \exp(4/x_e), \quad \text{and} \quad u_\theta(\lambda,\theta) = 0, \tag{45}$$

where

$$b(x) = \begin{cases} 0 & \text{if } x \leq 0, \\ \exp(-1/x) & \text{if } 0 < x. \end{cases} \tag{46}$$

and

$$x(\theta) = x_e \frac{(\theta - \theta_b)}{(\theta_e - \theta_b)}. \tag{47}$$

For the purposes of our analysis, we choose

$$u_0 = \left(\frac{2\pi a}{12 \text{ days}} \right), \quad \theta_b = -\frac{\pi}{6}, \quad \theta_e = \frac{\pi}{2}, \quad \text{and} \quad x_e = 0.3, \tag{48}$$

where $a = 6.37122 \times 10^6$ m denotes the radius of the Earth. These choices lead to a flow field which at maximal velocity completes one revolution of the sphere over a period of 12 days, and is confined to be nonzero only in the range $\theta \in [\theta_b, \theta_b + \theta_e]$.

This wind field is particularly useful for testing tracer advection schemes, for several reasons. First, the wind field is infinitely smooth, implying that for a sufficiently smooth tracer field high-order numerical methods should achieve an optimal convergence rate. Second, the wind field is purely zonal, so the zonally integrated mass of any tracer field is not a function of time. Third, the wind field is strongly nonlinear, and so emphasizes errors which are not captured in the linear regime. Finally, this test is representative of motions we would expect to see in the Earth's atmosphere, such as upper atmospheric jets in the midlatitudes. Notably, for numerical methods which use the latitude-longitude grid this test case is much easier when the grid is aligned with the flow. On the cubed-sphere (or on any other quasi-unstructured grid) we do not have the luxury of grid alignment, so we expect that grid imprinting will generate additional model errors. Further, we expect that zonally-integrated tracer mass will vary over time.

We consider two possible tracer fields for our study. The first is the constant field $\psi = 1$. Although somewhat primitive, this tracer field will allow us to very clearly isolate errors in capturing the wind field, and avoids the inclusion of errors due to the reconstruction. The second field we consider is $\psi = u_\lambda / u_0$, which is purposely chosen to have smooth purely meridional variation consistent with the velocity field. This choice will allow us to verify that the reconstruction errors for a more physical choice of tracer field are still overwhelmed by geometric errors in approximating the upstream areas. Both fields are steady with time under the velocity field (45).

DOI: 10.1002/fld

3.1.2. Discussion. The normalized root mean square L_2 error measures are calculated in the tracer field via the usual global error norms,

$$L_2(\psi) = \sqrt{\frac{I\left[(\psi - \psi_T)^2\right]}{I\left[\psi_T^2\right]}}, \tag{49}$$

where ψ_T is the tracer field at the initial time (the steady-state solution) and I denotes an approximation to the global integral, given by

$$I[x] = \sum_{\text{all cells } k} x_k |\mathcal{Z}|_k, \tag{50}$$

with $|\mathcal{Z}|_k$ denoting the area of element k.

The error norms obtained from running the nonlinearly sheared flow test case with $\psi = 1$ are plotted in Figure 6 for the flux-form CSLAM scheme of [4] with 0, 1 and 4 additional nodes added along each flux edge. Under this scheme, edges are treated as straight line segments without modification. In these tests the time step is chosen to be 3600 s at c60 resolution, 1800 s at c120 resolution, 900 s at c240 resolution and 450 s at c480 resolution. The corresponding grid spacings are listed in Table II. The data point at c480 resolution shows clear evidence of a lower bound in the error norms likely caused by poor conditioning of the line integral formulation. The error norms show consistent second-order convergence under grid refinement regardless of the number of added flux nodes. Nonetheless, we do observe a consistent decrease in the error norms as a function of the number of nodes along each edge. Given the benign nature of the tracer field, these errors strongly suggest that the flux volumes are not resolved with sufficient accuracy. In Figure 7 we see that the error norms associated with the quadrature implementation of the CSLAM scheme again show sub-optimal second-order convergence. However, under the quadratic treatment of edges the error norms drop dramatically, with the c60 resolution scheme with the improved edge treatment even outperforming the c480 resolution results with straight line segments. Further, with the quadratic treatment of edges the error norms are super-convergent at near-fourth-order accuracy. However, the quadratic formulation still appears to suffer from the poor conditioning of the line integral formulation at high resolutions, as we observe near-perfect convergence with the quadrature-based fluxes but flawed results with the line integral formulation.

The deficiencies revealed by this test can also be observed in the standard CSLAM scheme of [3], which similarly exhibits second-order convergence regardless of the number of flux points or choice of Courant number. For the issues that arise from this test we surmise high-order accuracy can only be recovered from a high-order treatment of the upstream source region in semi-Lagrangian schemes.

To verify that the loss of accuracy also occurs for a non-constant tracer field, we test the smooth tracer field $\psi = u_\lambda / u_0$. The results from this test can be seen in Figure 8 for the formulations of CSLAM described in this paper. The sub-optimal convergence rate is again apparent without quadratic edges, but is immediately recovered when quadratic edges are used. At lower resolutions the reconstruction error is more apparent, leading to error norms which do not significantly vary between the two edge treatments. In this case, the issues we observed with the constant tracer field

Prepared using fldauth.cls
DOI: 10.1002/fld

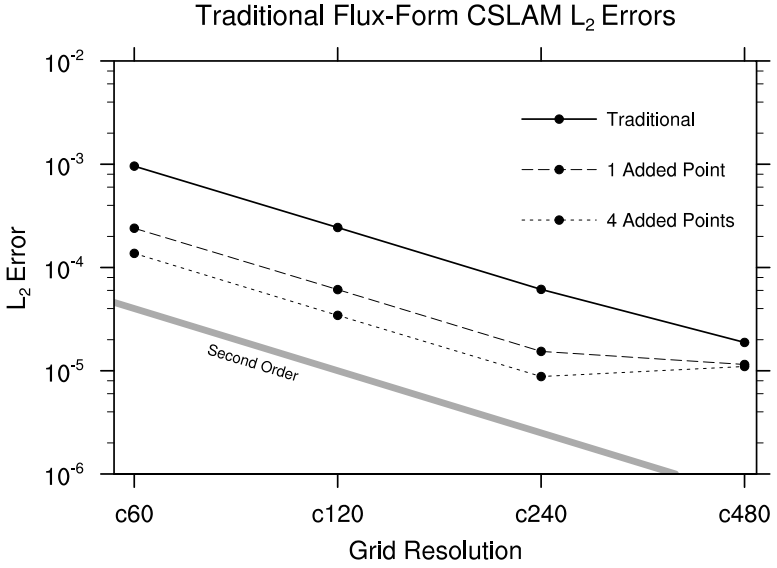

Figure 6. Normalized L_2 errors in the tracer field ψ for the nonlinearly sheared jet (at $t = 12$ days) for the traditional flux-form CSLAM schemes [4] with 0, 1 and 4 added flux points per edge and tracer field $\psi = 1$.

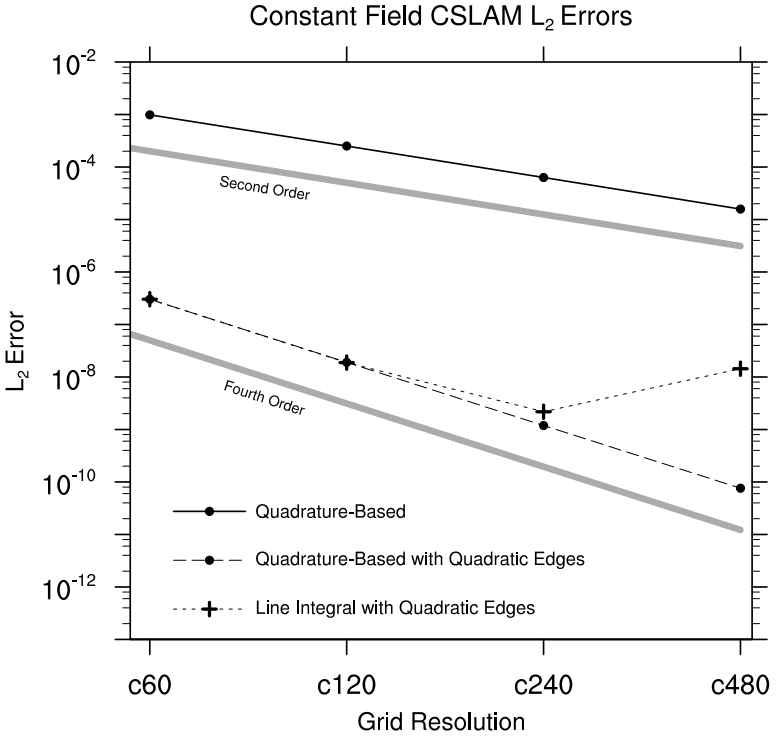

Figure 7. Normalized L_2 errors in the tracer field ψ for the nonlinearly sheared jet (after 12 days) test with initial tracer distribution $\psi = 1$. Errors from both quadrature-based and line integral-based schemes with quadratic upstream flux edges are shown.

at high resolutions do not seem to affect the line integral scheme, although they will likely appear at higher resolutions.

Based on these results, one may wonder if a quadratic representation of flux edges will also improve results in other known advection tests. In fact, the solid-body rotation test of [14] is

DOI: 10.1002/fld

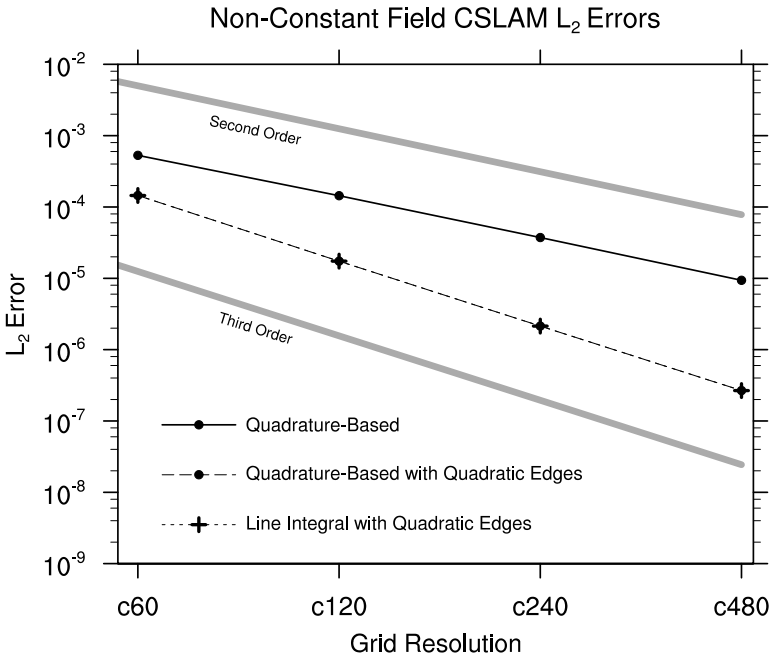

Figure 8. Normalized L_2 errors in the tracer field ψ for the nonlinearly sheared jet (after 12 days) test with initial tracer distribution $\psi = u_\lambda / u_0$. Errors from both quadrature-based and line integral-based schemes with quadratic upstream flux edges are shown. Both schemes with quadratic edges have roughly identical errors and hence appear atop one another in this plot.

completely unaffected by the improved resolution of the flux region. In this case, the upstream source region can be bounded exactly using great circle arcs, suggesting that piecewise linear boundaries are effectively optimal. Another popular test is the deformation flow test of [6] with either gaussian hills or cosine bells. For this test the error norms do not decrease under the improved treatment of flux boundaries, suggesting that the nonlinear shear in the wind field is sufficiently benign so as not lead to divergent errors that overcome the reconstruction errors at the tested resolutions. This result can be confirmed by running the deformational flow test with $q = 1$ (effectively removing the reconstruction errors from the test), in which case there is again a degradation in the formal order of accuracy of the method to second order (results not shown) without the quadratic treatment of edges. However, at sufficiently high resolution divergent errors should overwhelm reconstruction errors and consequently we expect the scheme will again drop to second-order accuracy.

3.2. Barotropic Instability

The shallow-water barotropic instability test case of [13] consists of a zonal jet with compact support at a latitude of $45°$, with a latitudinal profile roughly analogous to a much stronger version of test case 3 of [14]. A small height perturbation is added atop the jet which leads to the controlled formation of an instability in the flow. Consequently, as the flow field evolves we observe many realistic atmospheric dynamical features including sharp fronts and regions of enhanced vorticity. The wind field after 5 days from a shallow-water simulation at c160 resolution is depicted in Figure 9. As observed by [15], this test case is particularly difficult for models using the cubed-sphere to handle. Since the jet is significantly stronger than test case 3 of [14], is aligned in such a way that

Prepared using fldauth.cls
DOI: 10.1002/fld

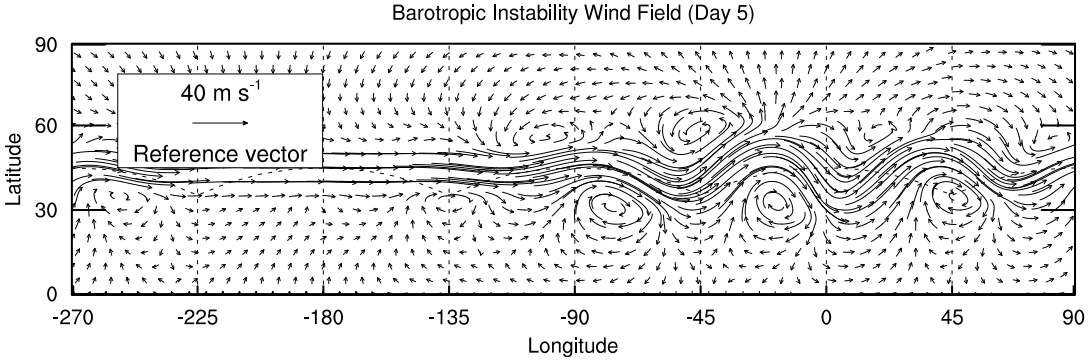

Figure 9. Wind field from the barotropic instability test at day 5. The maximum wind speed in the zonal jet is approximately 85 m s^{-1}.

it passes over cubed-sphere panel edges eight times, and is driven by a relatively mild perturbation, the wave number four grid forcing of the cubed-sphere grid is usually apparent in shallow-water simulations of this flow when the grid is coarser than c100 (which corresponds to a grid spacing of approximately 100 km).

To test the quadrature-based flux-form CSLAM transport scheme we treat the height field from [13] as a tracer field and passively advect it with prescribed winds from a shallow-water simulation that are updated at every timestep. We use the quadrature-based flux-form CSLAM scheme both without the quadratic correction (section 2.4) and with the quadratic correction (section 2.5). Further, we run at a resolution of c160 (~ 62.5 km as listed in Table II) with a time step of $\Delta t = 50\ s$ for 5 days. The height field after 5 days is then plotted in Figure 10, along with a high-order finite-volume reference solution obtained from the MCore shallow-water model described in [16, 17]. The implementation with the quadratic correction (Figure 10c) matches very closely with the reference solution, and shows no visually apparent indications of grid imprinting. On the other hand, although there is a rough correspondence between the solution without the quadratic correction (Figure 10b) and the reference solution, we observe clear discrepancies between these results, many of which appear to be driven by the underlying grid. In particular, grid imprinting is most readily apparent where the zonal jet passes over the cubed-sphere corners at both -225° and -135° degrees longitude. As a consequence, this test clearly identifies a benefit of the quadratic correction.

4. CONCLUSIONS

In this paper we have reformulated the flux-form semi-Lagrangian advection scheme of [4] using quadrature to compute the integral over flux volumes. An improved approach using quadratics to represent the edges of the upstream source region has also been implemented for both the quadrature formulation and line integral formulation of CSLAM. The new approach requires one additional trajectory calculation per flux edge, which roughly triples the number of trajectories that must be computed to obtain the upstream source areas. However, since these trajectories only need to be computed once at each time step, the added cost is small when transporting multiple tracers.

We have studied an analytic test case for tracer advection on the sphere that exhibits nonlinear wind shear analogous to the Earth's jet stream. This test has shown a deficiency in versions of

DOI: 10.1002/fld

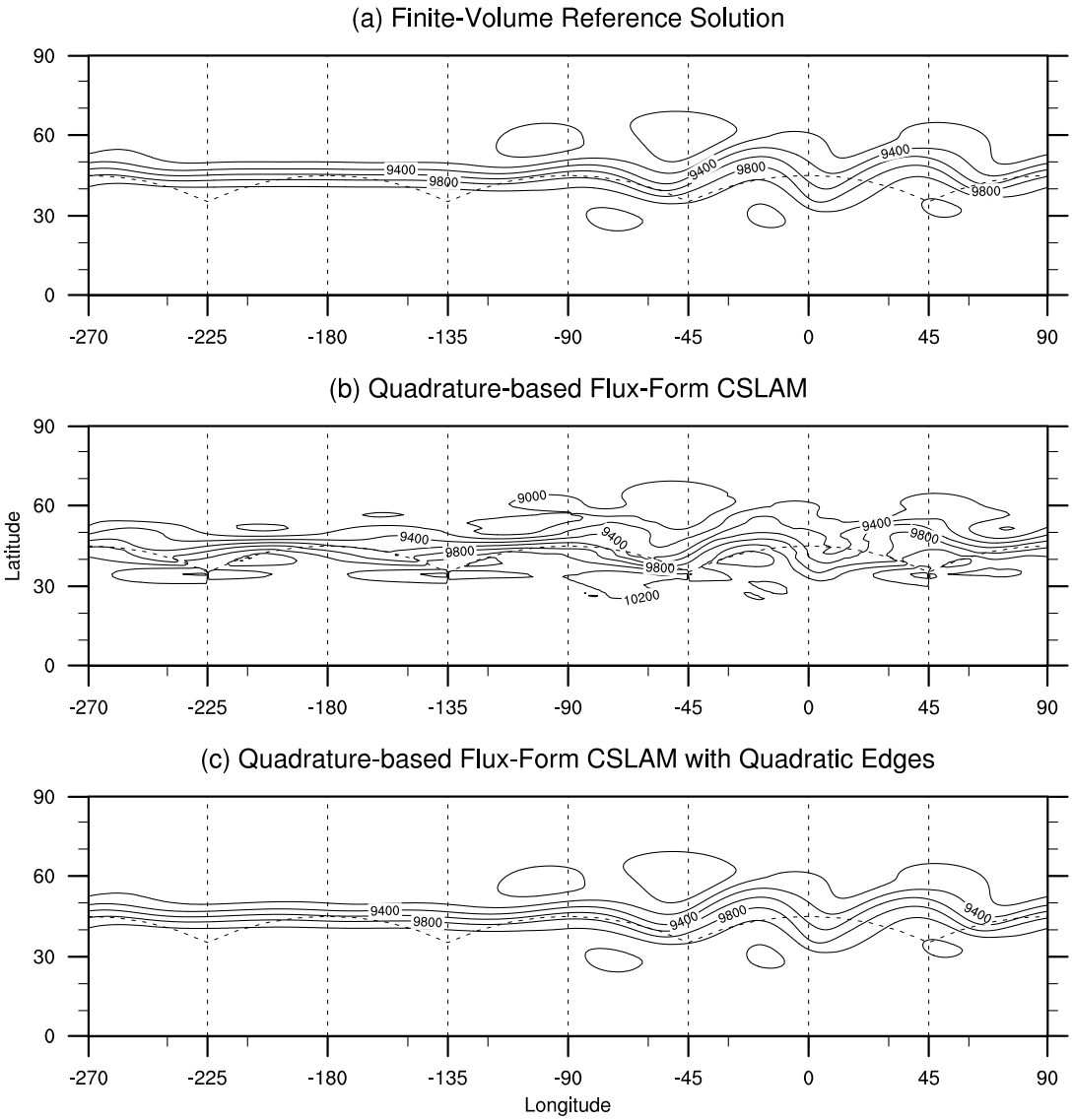

Figure 10. Height field from the barotropic instability test at day 5, as obtained from (a) the high-order finite-volume reference solution of [16], (b) the quadrature-based flux-form CSLAM transport scheme described in section 2.4 and (c) the quadrature-based flux-form CSLAM transport scheme with the quadratic correction, described in section 2.5. The height field is shown from 9000 m (northernmost enclosed contours) to 10200 m (southernmost enclosed contours) in increments of 200 m.

CSLAM that approximate upstream source regions using straight line segments which leads to a substantial worsening of observed errors and a decrease in the scheme's convergence rate from third-order to second-order. The quadratic treatment of the upstream edges was observed to substantially improve the error norms on this test and returned the convergence rate to third-order. This error is only revealed when a strong nonlinear shear is present in the flow, and so is often missed by other standardized tests. We have also studied a test case which mimics tracer transport in a barotropic instability, which reveals clear grid imprinting when using line segments to approximate the upstream flux volume. These errors are apparent even with a relatively fine grid spacing, but are removed when the quadratic correction is applied to the transport scheme.

Prepared using fldauth.cls
DOI: 10.1002/fld

ACKNOWLEDGEMENT

Support for this work has been provided by the Office of Science, U.S. Department of Energy, Award No. DE-SC0003990 and a University of Michigan Rackham Predoctoral Fellowship. The National Center for Atmospheric Research is sponsored by the National Science Foundation.

A. THE RECONSTRUCTION PROCEDURE

In the finite-volume formulation only averaged values of the state variables are stored within each element. That is, for each element $\mathcal{Z}_{i,j}$ we know the element average of the tracer field $\overline{\overline{\psi}}_{i,j}$, defined by

$$\overline{\overline{\psi}}_{i,j} = \frac{1}{|\mathcal{Z}|_{i,j}} \int_{\mathcal{Z}_{i,j}} \psi dV, \tag{51}$$

where $|\mathcal{Z}|_{i,j}$ is the element area. Here ψ denotes an arbitrary conserved variable, which can either be the fluid density ρ or the mass of a specific tracer $h\phi$, for a mixing ratio ϕ. The volume element is $dV = J_{\alpha\beta} d\alpha d\beta$ where the equiangular metric Jacobian $J_{\alpha\beta}$ is given by

$$J_{\alpha\beta} = \frac{(1+\tan^2\alpha)(1+\tan^2\beta)}{(1+\tan^2\alpha+\tan^2\beta)^{3/2}}. \tag{52}$$

Since only element-averaged information is known, an accurate reconstruction of the sub-grid-scale distribution of each state variable can only be obtained by using information from neighboring elements. By utilizing second-order approximations to the first and second derivatives of a reconstruction, standard finite-difference formula can be used to attain up to third-order accuracy. Such an approach has been used by [3] in the upstream element-integrated semi-Lagrangian formulation of the CSLAM scheme. The approach discussed here simplifies the reconstruction strategy of [18] by not enforcing that the integrated mass within an element equals the integrated mass of the sub-grid-scale reconstruction (the cell-averaged property). This property is not needed for incremental remap schemes in flux-form, since conservation is automatically enforced in the formulation. In fact, enforcement of this criteria does not even improve error norms since the maximum difference between these reconstructions is always within the $O(\Delta\alpha^3)$ truncation error of the scheme. Other reconstruction options have been implemented, including the approach of [19] which enforces continuity and the cell-averaged property; however, this method is significantly more expensive than the approach described here and does not lead to more accurate results.

The reconstruction strategy proceeds as follows. The stencil we use in the reconstruction step is depicted in Figure 11. First and second derivatives are calculated using standard finite-difference formulae, which leads to approximations which are $O(\Delta\alpha^2)$ accurate.

$$D_\alpha \psi_{i,j} = \frac{-\overline{\overline{\psi}}_{i+2,j} + 8\overline{\overline{\psi}}_{i+1,j} - 8\overline{\overline{\psi}}_{i-1,j} + \overline{\overline{\psi}}_{i-2,j}}{12\Delta\alpha}, \tag{53}$$

$$D_\beta \psi_{i,j} = \frac{-\overline{\overline{\psi}}_{i,j+2} + 8\overline{\overline{\psi}}_{i,j+1} - 8\overline{\overline{\psi}}_{i,j-1} + \overline{\overline{\psi}}_{i,j-2}}{12\Delta\alpha}, \tag{54}$$

DOI: 10.1002/fld

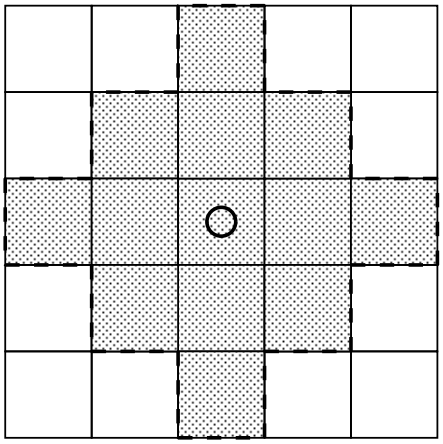

Figure 11. A depiction of the stencil used for computing the third-order sub-grid-scale reconstruction on the cubed-sphere.

$$D_{\alpha\alpha}\psi_{i,j} = \frac{-\overline{\overline{\psi}}_{i+2,j} + 16\overline{\overline{\psi}}_{i+1,j} - 30\overline{\overline{\psi}}_{i,j} + 16\overline{\overline{\psi}}_{i-1,j} - \overline{\overline{\psi}}_{i-2,j}}{24\Delta\alpha^2}, \quad (55)$$

$$D_{\alpha\beta}\psi_{i,j} = \frac{\overline{\overline{\psi}}_{i+1,j+1} - \overline{\overline{\psi}}_{i-1,j+1} - \overline{\overline{\psi}}_{i+1,j-1} + \overline{\overline{\psi}}_{i-1,j-1}}{4\Delta\alpha^2}, \quad (56)$$

$$D_{\beta\beta}\psi_{i,j} = \frac{-\overline{\overline{\psi}}_{i,j+2} + 16\overline{\overline{\psi}}_{i,j+1} - 30\overline{\overline{\psi}}_{i,j} + 16\overline{\overline{\psi}}_{i,j-1} - \overline{\overline{\psi}}_{i,j-2}}{24\Delta\alpha^2}. \quad (57)$$

The final step in building a third-order reconstruction relies on obtaining a $O(\Delta\alpha^3)$ approximation to the centerpoint value of ψ. Here we follow the deconvolution procedure of [20]. Using this strategy, over a sufficiently smooth field element-averages can be used to obtain an approximation to the centerpoint value, according to

$$\psi_{(0)} = \overline{\overline{\psi}} - \frac{\Delta\alpha^4}{12|\mathcal{Z}|}\left(\frac{\partial\psi}{\partial\alpha}\frac{\partial J_{\alpha\beta}}{\partial\alpha} + \frac{\partial\psi}{\partial\beta}\frac{\partial J_{\alpha\beta}}{\partial\beta}\right) - \frac{\Delta\alpha^2}{24}\left(\frac{\partial^2\psi}{\partial\alpha^2} + \frac{\partial^2\psi}{\partial\beta^2}\right). \quad (58)$$

If $\overline{\overline{\psi}}_{i,j}$ is known to at least fourth-order accuracy and the remaining derivative terms are known to at least $O(\Delta\alpha^2)$, this formula leads to a fourth-order-accurate approximation of $\psi_{(0)i,j}$, the element-centered value of ψ in element (i,j). In this formulation, the derivatives of the Jacobian are computed analytically and stored for later use. Hence, on substituting approximations to these derivatives we obtain the fourth-order-accurate approximation

$$\psi_{(0)i,j} = \overline{\overline{\psi}}_{i,j} - \frac{\Delta\alpha^4}{12|\mathcal{Z}|_{i,j}}\left(D_\alpha\psi\frac{\partial J_{\alpha\beta}}{\partial\alpha} + D_\beta\psi\frac{\partial J_{\alpha\beta}}{\partial\beta}\right) - \frac{\Delta\alpha^2}{24}\left(D_{\alpha\alpha}\psi + D_{\beta\beta}\psi\right). \quad (59)$$

DOI: 10.1002/fld

A.1. Filtering the reconstruction

When $q = h\phi$, the reconstruction must be filtered so that ϕ satisfies the constraint $\phi \in [0, 1]$. Consequently, we can extract the reconstruction for ϕ using the following differential relationships:

$$\begin{aligned}
\phi_{(0)} &= \frac{(h\phi)_{(0)}}{h_{(0)}}, \\
D_\alpha \phi &= \frac{1}{h_{(0)}} \left[D_\alpha (h\phi) - \phi_{(0)} D_\alpha h \right], \\
D_\beta \phi &= \frac{1}{h_{(0)}} \left[D_\beta (h\phi) - \phi_{(0)} D_\beta h \right], \\
D_{\alpha\alpha} \phi &= \frac{1}{h_{(0)}} \left[D_{\alpha\alpha} (h\phi) - 2 D_\alpha \phi D_\alpha h - \phi_{(0)} D_{\alpha\alpha} h \right], \\
D_{\alpha\beta} \phi &= \frac{1}{h_{(0)}} \left[D_{\alpha\beta} (h\phi) - D_\alpha \phi D_\beta h - D_\beta \phi D_\alpha h - \phi_{(0)} D_{\alpha\beta} h \right], \\
D_{\beta\beta} \phi &= \frac{1}{h_{(0)}} \left[D_{\beta\beta} (h\phi) - 2 D_\beta \phi D_\beta h - \phi_{(0)} D_{\beta\beta} h \right].
\end{aligned}$$

Observe that this reconstruction satisfies mass / tracer consistency; that is, when $\phi = 1$ the reconstructions of h and $(h\phi)$ will be identical and hence the reconstruction of ϕ is exactly the constant function $\phi(\alpha, \beta) = 1$. Further, since the formulae above are exact, this equivalence preserves the order of accuracy of the underlying reconstruction.

The advection algorithm currently supports two filters to maintain desirable properties of the reconstruction. A positivity-preserving limiter is available to avoid spurious negative values due to undershoots in the reconstruction and a stricter monotonic limiter is available for removing all unphysical oscillations. The limiters follow the approach of [21], wherein extreme values of the sub-grid-scale reconstruction are detected and the reconstruction is scaled so that these extreme values fit within some predefined range. For the positivity-preserving limiter the range is simply chosen to be $[0, +\infty]$, implying maximum values of the reconstruction are left untouched while minimum values are cropped to zero if they are anywhere negative. For many tracer quantities the positivity-preserving limiter is sufficient since overshoots are on the order of the reconstruction, and hence if the element-averaged tracer concentration $\overline{\overline{\phi}} \ll 1$ it follows that the reconstructed concentration $\phi(\alpha, \beta)$ will never exceed 1. For the monotonicity-preserving limiter, the range is chosen to be $[\phi_{min}, \phi_{max}]$, where

$$\begin{aligned}
\phi_{min} &= \min_{\mathcal{N}_k} \overline{\overline{(h\phi)}}_k / \overline{\overline{h}}_k, \\
\phi_{max} &= \max_{\mathcal{N}_k} \overline{\overline{(h\phi)}}_k / \overline{\overline{h}}_k,
\end{aligned}$$

and $\mathcal{N}_k$ is the set of all neighboring elements to element k, including element k itself. On a regular Cartesian grid, even diagonal neighbors are considered when determining the minimum and maximum value of the scalar field, so in total 9 elements are used. It can be shown that under a sufficiently strict CFL condition (usually Courant number $< \frac{1}{2}$) the limiting procedure described above can be used to avoid spurious overshoots and undershoots in the numerical method while retaining high-order accuracy in smooth regions.

A.2. Conversion of the reconstruction to Gnomonic coordinates

When integrating over flux areas, integration is performed in Gnomonic coordinates. Hence, the derivatives in equiangular (α, β) coordinates must be converted to Gnomonic derivatives in (X, Y). We initially convert

DOI: 10.1002/fld

first derivatives to Gnomonic coordinates via

$$D_X \psi_{i,j} = \frac{1}{1+X^2} D_\alpha \psi_{i,j}, \tag{60}$$

$$D_Y \psi_{i,j} = \frac{1}{1+Y^2} D_\beta \psi_{i,j}, \tag{61}$$

and then second derivatives using

$$D_{XX} \psi_{i,j} = \frac{1}{1+X^2} \left(-X D_X \psi_{i,j} + \frac{1}{1+X^2} D_{\alpha\alpha} \psi_{i,j} \right), \tag{62}$$

$$D_{XY} \psi_{i,j} = \frac{1}{(1+X^2)(1+Y^2)} D_{\alpha\beta} \psi_{i,j}, \tag{63}$$

$$D_{YY} \psi_{i,j} = \frac{1}{1+Y^2} \left(-Y D_Y \psi_{i,j} + \frac{1}{1+Y^2} D_{\beta\beta} \psi_{i,j} \right). \tag{64}$$

Upon computing all gnomonic derivatives, the third-order reconstruction within element $\mathcal{Z}_{i,j}$ takes the form

$$\begin{aligned} \psi_{i,j}(\mathbf{X}) = \; & \psi_{(0)i,j} + (X - X_i) D_X \psi_{i,j} + (Y - Y_j) D_Y \psi_{i,j} \\ & + (X - X_i)^2 \frac{D_{XX} \psi_{i,j}}{2} + (X - X_i)(Y - Y_j) D_{XY} \psi_{i,j} + (Y - Y_j)^2 \frac{D_{YY} \psi_{i,j}}{2}, \end{aligned} \tag{65}$$

where $\mathbf{X} = (X, Y)$ is the vector form of the gnomonic coordinate.

The approach described above cannot be applied directly for elements in the vicinity of panel edges, since accurate reconstruction relies on all neighboring element averages being defined in the same coordinate system. To avoid this problem, neighboring panel information is remapped into "halo" regions surrounding each panel which are defined in the same coordinate system. This approach relies on an accurate remapping scheme, such as the one described in [16].

A.3. Conversion to a global coordinate system

The reconstruction coefficients $c_{(p,q)}$ which are then required in the expansion (16) are computed by expanding (66) and collecting like terms. This procedure leads to the following set of reconstruction coefficients:

$$\begin{aligned} c_{(0,0)} = \; & \psi_{(0)i,j} - X_i D_X \psi_{i,j} - Y_j D_Y \psi_{i,j} \\ & + X_i^2 \frac{D_{XX} \psi_{i,j}}{2} + X_i Y_j D_{XY} \psi_{i,j} + Y_j^2 \frac{D_{YY} \psi_{i,j}}{2}, \end{aligned} \tag{66}$$

$$c_{(1,0)} = D_X \psi_{i,j} - X_i D_{XX} \psi_{i,j} - Y_j D_{XY} \psi_{i,j}, \tag{67}$$

$$c_{(0,1)} = D_Y \psi_{i,j} - Y_j D_{YY} \psi_{i,j} - X_i D_{XY} \psi_{i,j}, \tag{68}$$

$$c_{(2,0)} = \frac{D_{XX} \psi_{i,j}}{2}, \tag{69}$$

$$c_{(1,1)} = D_{XY} \psi_{i,j}, \tag{70}$$

$$c_{(0,2)} = \frac{D_{YY} \psi_{i,j}}{2}. \tag{71}$$

REFERENCES

1. Lauritzen PH, Ullrich PA, Nair RD. Atmospheric Transport Schemes: Desirable Properties and a Semi-Lagrangian View on Finite-Volume Discretizations. *Numerical Techniques for Global Atmospheric Models, Lecture Notes in Computational Science and Engineering*, vol. 80, Springer, 2011; 185–250.

DOI: 10.1002/fld

2. Dukowicz JK, Baumgardner JR. Incremental Remapping as a Transport/Advection Algorithm. *J. Comput. Phys.* May 2000; **160**:318–335, doi:10.1006/jcph.2000.6465.
3. Lauritzen PH, Nair RD, Ullrich PA. A conservative semi-Lagrangian multi-tracer transport scheme (CSLAM) on the cubed-sphere grid. *J. Comp. Phys.* 2010; **229**:1401–1424.
4. Harris LM, Lauritzen PH, Mittal R. A flux-form version of the conservative semi-Lagrangian multi-tracer transport scheme (CSLAM) on the cubed sphere grid. *J. Comput. Phys.* 2011; **230**:1215–1237, doi:10.1016/j.jcp.2010.11.001.
5. Lauritzen PH, Erath C, Mittal R. On simplifying 'incremental remap'-type transport schemes. *J. Comput. Phys.* 2011; **230**:7957 – 7963, doi:10.1016/j.jcp.2011.06.030.
6. Nair RD, Lauritzen PH. A class of deformational flow test cases for linear transport problems on the sphere. *J. Comput. Phys.* 2010; **229**:8868–8887, doi:10.1016/j.jcp.2010.08.014.
7. Neale RB, Chen CC, Gettelman A, Lauritzen PH, Park S, Williamson DL, Conley AJ, Garcia R, Kinnison D, Lamarque JF, *et al.*. Description of the NCAR Community Atmosphere Model (CAM 5.0). *NCAR Technical Note NCAR/TN-486+STR*, National Center for Atmospheric Research, Boulder, Colorado June 2010. 268 pp., available from http://www.cesm.ucar.edu/models/cesm1.0/cam/.
8. Hirt C, Amsden A, Cook J. An arbitrary Lagrangian-Eulerian computing method for all flow speeds. *J. Comput. Phys.* 1974; **14**(3):227–253, doi:10.1016/0021-9991(74)90051-5. URL `http://www.sciencedirect.com/science/article/pii/0021999174900515`.
9. Sadourny R. Conservative finite-difference approximations of the primitive equations on quasi-uniform spherical grids. *Mon. Weather Rev.* 1972; **100**:136–144.
10. Ronchi C, Iacono R, Paolucci PS. The "cubed sphere": A new method for the solution of partial differential equations in spherical geometry. *J. Comput. Phys.* 1996; **124**(1):93–114.
11. McGregor JL. Economical Determination of Departure Points for Semi-Lagrangian Models. *Mon. Weather Rev.* 1993; **121**:221, doi:10.1175/1520-0493(1993)121⟨0221:EDODPF⟩2.0.CO;2.
12. Durran DD. *Numerical Methods for Wave Equations in Geophysical Fluid Dynamics*. Springer-Verlag, 1998.
13. Galewsky J, Scott RK, Polvani LM. An initial-value problem for testing numerical models of the global shallow-water equations. *Tellus Series A* 2004; **56**:429–440, doi:10.1111/j.1600-0870.2006.00192.x"class="ref.
14. Williamson D, Drake J, Hack J, Jakob R, Swarztrauber P. A standard test set for numerical approximations to the shallow water equations in spherical geometry. *J. Comput. Phys.* 1992; **102**:211–224.
15. St-Cyr A, Jablonowski C, Dennis JM, Tufo HM, Thomas SJ. A comparison of two shallow-water models with nonconforming adaptive grids. *Mon. Weather Rev.* 2008; **136**:1898–1922, doi:10.1175/2007MWR2108.1.
16. Ullrich PA, Jablonowski C, van Leer B. High-order finite-volume models for the shallow-water equations on the sphere. *J. Comput. Phys.* 2010; **229**:6104–6134.
17. Ullrich PA, Jablonowski C. MCore: A Non-hydrostatic Atmospheric Dynamical Core Utilizing High-Order Finite-Volume Methods. *J. Comput. Phys.* 2012; Revised Jan 2012.
18. Ullrich PA, Lauritzen PH, Jablonowski C. Geometrically exact conservative remapping (GECoRe): Regular latitude-longitude and cubed-sphere grids. *Mon. Weather Rev.* 2009; **137**:1721–1741.
19. Rančić M. Semi-Lagrangian piecewise biparabolic scheme for two-dimensional horizontal advection of a passive scalar. *Monthly Weather Review* July 1992; **120**:1394–1405.
20. Barad M, Colella P. A fourth-order accurate local refinement method for Poisson's equation. *J. Comput. Phys.* 2005; **209**:1–18, doi:10.1016/j.jcp.2005.02.027.
21. Barth T, Jespersen D. The design and application of upwind schemes on unstructured meshes. *Proc. AIAA 27th Aerospace Sciences Meeting, Reno*, 1989.